IOP Publishing Phys. Med. Biol. 71 (2026) 015001 https://doi.org/10.1088/1361-6560/ae2b4a

Physics in Medicine & Biology

IPEM Institute of Physics and Engineering in Medicine

PAPER

A compact depth-of-interaction time-of-flight detector panel dedicated for organ-specific PET scanner

OPEN ACCESS

RECEIVED
20 September 2025

REVISED
3 December 2025

ACCEPTED FOR PUBLICATION
10 December 2025

PUBLISHED
22 December 2025

Mehdi Amini[1], **Abdollah Saberi Manesh**[1], **Katayoun Doroud**[2], **Hossein Arabi**[1] and **Habib Zaidi**[1,3,4,5,*]

[1] Division of Nuclear Medicine and Molecular Imaging, Geneva University Hospital, Geneva, Switzerland
[2] Picotech, 01630 St Genis Pouilly, France
[3] Department of Nuclear Medicine and Molecular Imaging, University of Groningen, University Medical Center Groningen, Groningen, The Netherlands
[4] Department of Nuclear Medicine, University of Southern Denmark, Odense, Denmark
[5] University Research and Innovation Center, Óbuda University, Budapest, Hungary
[*] Author to whom any correspondence should be addressed.

E-mail: habib.zaidi@hcuge.ch

Keywords: PET, depth of interaction, time-of-flight, organ-dedicated PET, detector panel

Supplementary material for this article is available online

Abstract

Objective. Dedicated positron emission tomography (PET) scanners designed for specific organs or clinical applications require compact detector modules with high depth-of-interaction (DOI) and time-of-flight (TOF) capabilities. In this study, we present the design and evaluation of a compact, ready-to-use PET detector panel optimized for such scanners. *Approach.* The panel, measuring 98.4×104.2 mm^2, comprises a 4×3 array of four-layer, dual-readout detector towers. Detector towers operate in side-irradiation configuration, thereby enabling DOI measurement across the layers, while axial positioning is derived from the dual-ended readout. Each tower is built from a $8 \times 4 \times 1$ array of $2.05 \times 4.4 \times 30$ mm^3 Lutetium Fine Silicate (LFS) crystals, axially coupled to strip-shaped multi-pixel photon counters, with both ends of each strip read out through independent electronic channels. A high-speed electronic readout system based on the picoTDC application-specific integrated circuit was developed to enable precise timing and amplitude measurements. Calibration and performance evaluations were conducted under realistic and scaled conditions. A full-range energy calibration was performed at crystal-level using multiple gamma-emitting isotopes to linearize the detector's response and extract energy resolution. Calibration for axial-positioning along the length of the crystals (between two readout ends) was achieved through a simple flood irradiation-based method, eliminating the need for point-specific irradiations. *Main results.* Average energy resolutions of 14.2%, 14.3%, 15.3%, and 15.4% were achieved for crystals in layers 1 through 4, respectively. DOI and transaxially positioning steps of 4.4 mm, and 2.05 mm, respectively are obtainable based on layer and crystal pitch. The measured axial spatial resolutions were 3.78 mm, 3.84 mm, 4.01 mm, and 4.78 mm full-width-half-maximum for layers 1 through 4, respectively. TOF resolution averaged 196 ± 7 ps for layer 1–1 pair, gradually degrading to 220 ± 17 ps for layer 4–4 pairs. *Significance.* Balancing performance, scalability, and manufacturability, this detector panel offers a practical and easily calibratable solution for next-generation organ-dedicated PET systems with DOI-TOF capability.

1. Introduction

Positron emission tomography (PET) has become an indispensable imaging modality in precision medicine, offering non-invasive, *in vivo* visualization and quantification of physiological processes (El Ouaridi *et al* 2024). Conventional whole-body PET scanners are designed to provide reproducible and quantitatively accurate images across diverse clinical indications. In addition to imaging performance, these systems are often optimized for accessibility, cost-effectiveness, ease of use, serviceability, spatial footprint, and energy consumption (Sanaat *et al* 2024). However, achieving excellence in all these dimensions simultaneously is inherently constrained by trade-offs. To overcome these limitations and to better address specific clinical or research needs, a recent and growing trend in PET instrumentation is the development of organ- or application-dedicated PET scanners (Zaidi *et al* 2024). By tailoring design parameters to a narrower range of imaging requirements, such systems can prioritize and enhance selected performance metrics that are of critical importance for particular use cases (Catana 2019). However, these dedicated PET systems often require a distinct line of technological development encompassing detector design, system architecture, and image reconstruction strategies (Gonzalez and Gonzalez-Montoro 2024). At the heart of any PET scanner lies its detector system, responsible for capturing the 511 keV annihilation photons. The design and performance of the detectors fundamentally determine the scanner's capabilities most notably its spatial resolution and uniformity across the field-of-view, plus timing resolution and energy resolution (Zatcepin and Ziegler 2023).

One of the main motivations behind dedicated PET scanner development is to achieve higher spatial resolution for the organ of interest, which is commonly achieved by decreasing the gantry diameter or by bringing the detectors closer to the subject through alternative configurations, such as planar detector arrangements (Sanaat *et al* 2024). Reducing the distance between the patient and the detectors increases the system's sensitivity. Moreover, smaller gantry diameter or panel distance, reduces the impact of photon acollinearity, hence contributing to improved spatial resolution (Shibuya *et al* 2007). In addition to enhanced performance, compact scanner geometries offer several practical advantages including fewer detector elements, reduced manufacturing costs, and improved mobility (Sanaat *et al* 2024). However, these benefits come with a significant trade-off. As the detectors are positioned closer to the subject, a larger proportion of annihilation photons impact on the detector at oblique angles, which results in increased parallax error (Moses 2011). Detectors with depth of interaction (DOI) capability can mitigate this error (Mohammadi *et al* 2019b). DOI information enables more accurate line of response (LOR) estimation, making it an essential feature in detectors designed for dedicated PET systems (Razdevšek *et al* 2025).

Fast coincidence time resolution (CTR) is another critical performance metric for PET systems (Surti and Karp 2020). A precise CTR enables the use of a narrow coincidence time window, which is particularly beneficial for reducing random coincidences. Moreover, excellent timing resolution allows the system to exploit time-of-flight (TOF) information. By measuring the difference in arrival times of the two annihilation photons, TOF-capable PET systems can localize the annihilation event along the LOR with greater precision. This temporal localization leads to a significant improvement in image quality by enhancing the signal-to-noise ratio, which enables low-count or high-noise imaging (Schaart 2021). In essence, while DOI capability allows detectors to be positioned closer to the patient, increasing the number of detected true coincidences, TOF, in turn, makes each of these events more informative, providing additional spatial localization. Together, these capabilities move PET imaging closer to low-dose acquisitions (Conti and Bendriem 2019), which is another key motivation behind the development of dedicated PET scanners. It is also worth mentioning that these two capabilities are interrelated as DOI information can improve CTR. Together, DOI and TOF capabilities form the backbone of high-performance detector systems required for compact, high-precision organ-specific PET imaging systems.

PET detectors capable of providing both TOF and DOI information have been extensively reviewed (Yoshida and Yamaya 2024). The primary approaches for achieving simultaneous DOI and TOF capabilities include dual-readout (Liu *et al* 2022, Seo *et al* 2023, Weindel *et al* 2023, Jung *et al* 2024, Wang *et al* 2024, 2025), monolithic crystals (Borghi *et al* 2016, Gonzalez-Montoro *et al* 2022), light sharing (Pizzichemi *et al* 2019, LaBella *et al* 2021, Yoshida *et al* 2024), and side-readout (Cates and Levin 2018, Pourashraf *et al* 2024). Each of these approaches offers distinct advantages but also presents technical and practical challenges that continue to limit their widespread adoption. Monolithic crystals require complex and labor-intensive calibration procedures, which must be performed individually for each detector module. Furthermore, due to internal reflections at the crystal boundaries, event localization near the edges is often compromised (Gonzalez-Montoro *et al* 2021). Light-sharing detectors also demand intensive calibration and sophisticated signal processing algorithms. Their construction is often intricate and costly, presenting manufacturing challenges (LaBella *et al* 2021, Yoshida *et al* 2024). Side-readout schemes have demonstrated some of the highest reported performances in both TOF and DOI metrics (Watanabe *et al* 2021). However, these designs are inherently complex and expensive, primarily due to increased photodetector coverage and readout requirements. Signal multiplexing has been explored as a cost-reduction strategy, but it typically involves trade-offs in timing and spatial performance (Pourashraf *et al* 2024). Additionally, dead spaces occupied by the photodetectors between crystals in these configurations can degrade system sensitivity (Wang *et al* 2025).

Among the various approaches, dual-ended readout detectors remain the most straightforward solution for achieving DOI and TOF information (Yoshida and Yamaya 2024). Collecting scintillation light from both ends of the crystal enables achieving a high light collection efficiency, comparable to that of side-readout configurations (Yoshida and Yamaya 2024). Additionally, the proximity of the photodetectors to the interaction points, compared to single-ended designs, can lead to improved CTR (Mohammadi *et al* 2019a). Their primary drawback lies in the increased hardware cost. Several strategies have been proposed to address this limitation, including multiplexing readout via stripline configuration of SiPMs, enabling row and column position discrimination (Wang *et al* 2024), sparse SiPM coverage (Seo *et al* 2023), and axial readout architectures that utilize longer crystals (Weindel *et al* 2023).

In this study, we present the development and validation of a ready-to-use compact detector panel that can be readily adopted by manufacturers for the construction of various organ/purpose-dedicated PET systems. The panel consists of an array of 4-layered (for DOI) dual-readout (for axial positioning) detector towers, operating in side-irradiation mode, coupled to high-speed electronic readout units enabling TOF capability. The main contributions of this work can be summarized as follows:

(1) *Detector configuration:* the specific design of the detector towers provides a high degree of signal redundancy for each detected event, thus enhancing measurement precision by reducing statistical uncertainty and improving both spatial and temporal resolution.
(2) *Simplified flood-based calibration:* a major methodological contribution of this work is the development of an effortless calibration procedure based on a single uniform flood-irradiation acquisition, which circumvents the need for point-by-point irradiations typically required for the calibration of dual-readout detectors.
(3) *Intermediate-scale performance evaluation:* key detector-level performance metrics, including timing, spatial, and energy resolutions were assessed using a detector panel composed of multiple detector towers rather than an isolated crystal array under ideal laboratory conditions. Additional experimental design choices, such as placing a carbon-fiber bed on the detector panel in different tests, and performing acquisitions across varying temperature and power cycles, were implemented to emulate realistic data acquisition conditions. This ensures that the reported results better reflect practical system performance for potential future use.

Furthermore, this detector panel is currently being implemented by our team for the construction of a dual-panel prostate-dedicated PET scanner (ProVision), with system-level performance evaluation and imaging results to be reported in separate/subsequent publications.

2. Materials and methods

2.1. Detector configuration

The proposed detector panel consists of an array of four-layered dual-readout detector towers. Photographs of the proposed detector panel and the readout electronics are presented in figure 1. The panel contains 12 detector towers arranged in a 4 × 3 grid along *X* and *Z* directions, respectively (figure 2(a)). The full panel measures 98.4 × 104.2 mm^2 and the center-to-center distances between the towers are 26.8 mm and 37.1 mm, along the *X* and *Z* directions, respectively.

Detector towers operate in side-irradiation configuration, enabling DOI measurement across the layers, while axial positioning is derived from the dual-ended readout. The detector towers employ Lutetium Fine Silicate (LFS) scintillator crystals, characterized by a density of 7.35 g cm^{-3}, an attenuation length of 1.15 cm for 511 keV photons, and a refractive index of 1.81. Its light yield reaches approximately 80% of that of NaI(Tl), and a decay time of 36 ns, which is shorter than the 41 ns of more commonly used LYSO crystals (Doroud *et al* 2014). Supplementary table 1 summarizes the physical properties of LFS and LYSO crystals. A comparison of their CTR for 15 mm-long crystals, as reported in (Doroud *et al* 2014), showed that LFS achieved a CTR of 148 ps, outperforming LYSO, which recorded a CTR of 180 ps.

Each detector tower consists of a stack of 32 LFS crystals (figure 2(c)), forming a block with overall dimensions of 18 × 18 × 30 mm along the *X, Y,* and *Z* axes, respectively. The block is configured as an array of 8 crystals along the *X* axis, stacked in 4 layers along the *Y* axis. Each individual LFS crystal measures 2.05 × 4.4 × 30 mm. All surfaces are polished, and adjacent crystals are optically isolated using powdered barium sulfate ($BaSO_4$). Additionally, the four lateral surfaces are coated with $BaSO_4$ and an outer layer of E60 to enhance optical photon collection.

Two arrays of strip-shaped multi-pixel photon counter (SMPPC) silicon photomultipliers (SiPMs) (Hamamatsu, Japan) are attached to opposite sides of the detector (figure 1(c)) using EP601-LV epoxy

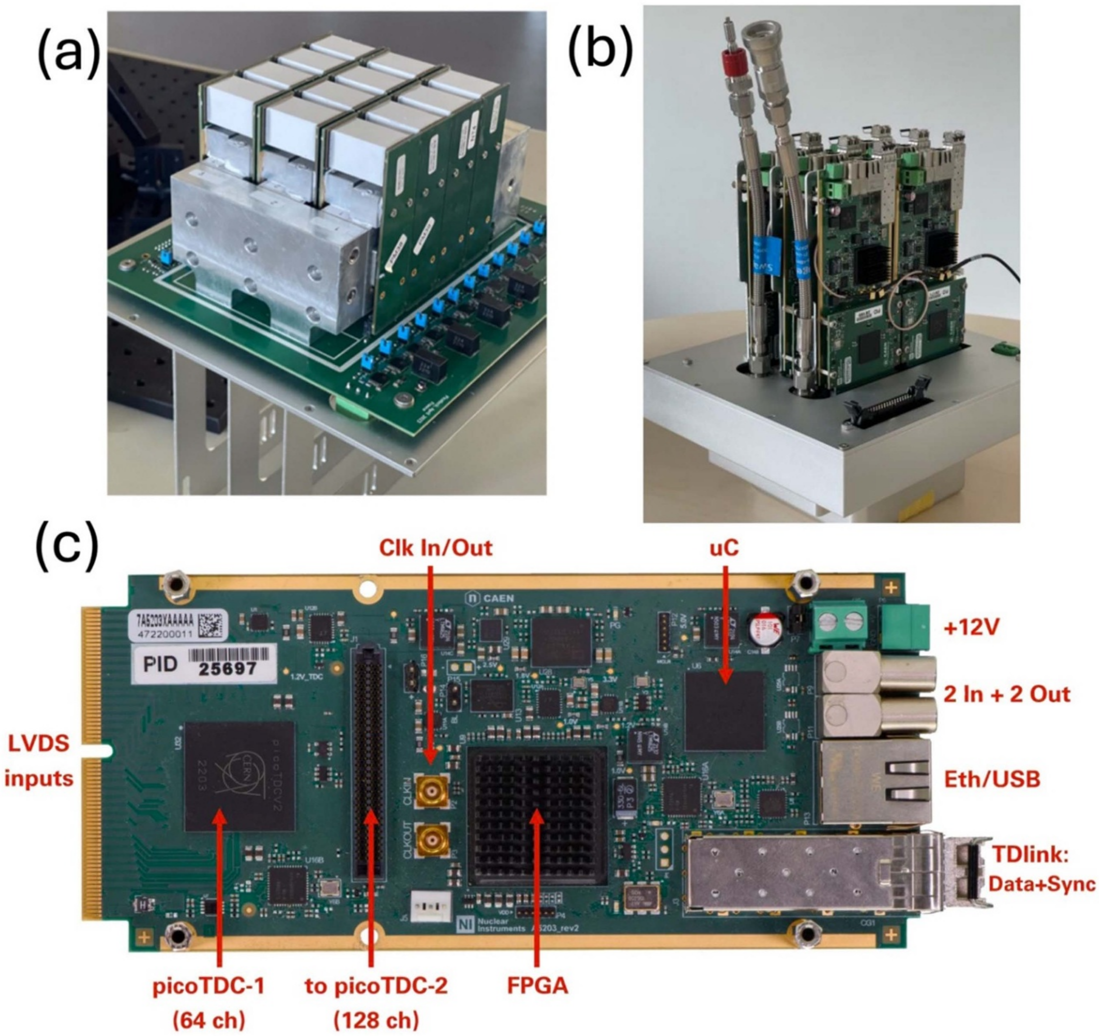

Figure 1. Photographs of the detector panel and its readout electronics. (a) Front view of the panel showing the crystal arrays. (b) Rear view of the panel showing the readout electronic cards. (c) A single readout electronic card with its main components highlighted.

glue (Polytec PT GmbH). Each SMPPC array consists of 16 strips mounted on a substrate, with a 0.08 mm gap between adjacent SMPPCs and a 0.25 mm gap between groups of four (layers). Each SMPPC features an active area of 18×1 mm^2 with single-photon avalanche diodes (SPADs) of 50×50 μm^2 and is read with 2 channels at its ends (Doroud *et al* 2021).

To simplify orientation and referencing, the sides of the detector tower are assigned directional (Dir) labels: the faces attached to the SMPPC arrays are referred to as North (N) and South (S), while the perpendicular ends of the SMPPCs are designated East (E) and West (W). Each layer (consequently each crystal) is attached to 4 SMPPCs at each end, thus read by 16 channels (each SMPPC is read by two channels) organized into four directional groups: NE, NW, SE, and SW.

2.2. Readout

Each SMPPC is read out from both ends with an ultra-fast amplifier discriminator, thus 64 channels are required to fully instrument a single detector tower. The power consumption is about 27 mW per channel. A closed loop water cooling system is used to dissipate this power. An onboard chip provides high-voltage power supply optimized for driving SMPPCs, which contains a temperature compensation function that constantly regulates the SMPPCs operation in environments with varying temperatures. All SMPPCs are operated at around 6 V overvoltage.

The readout operations are handled by the CAEN A5203B, part of the FERS-5200 (front-end readout system) electronics platform (figure 1(c)). It integrates two CERN picoTDC application-specific integrated circuits (ASICs) in a compact and scalable unit capable of high-resolution time of arrival (ToA)

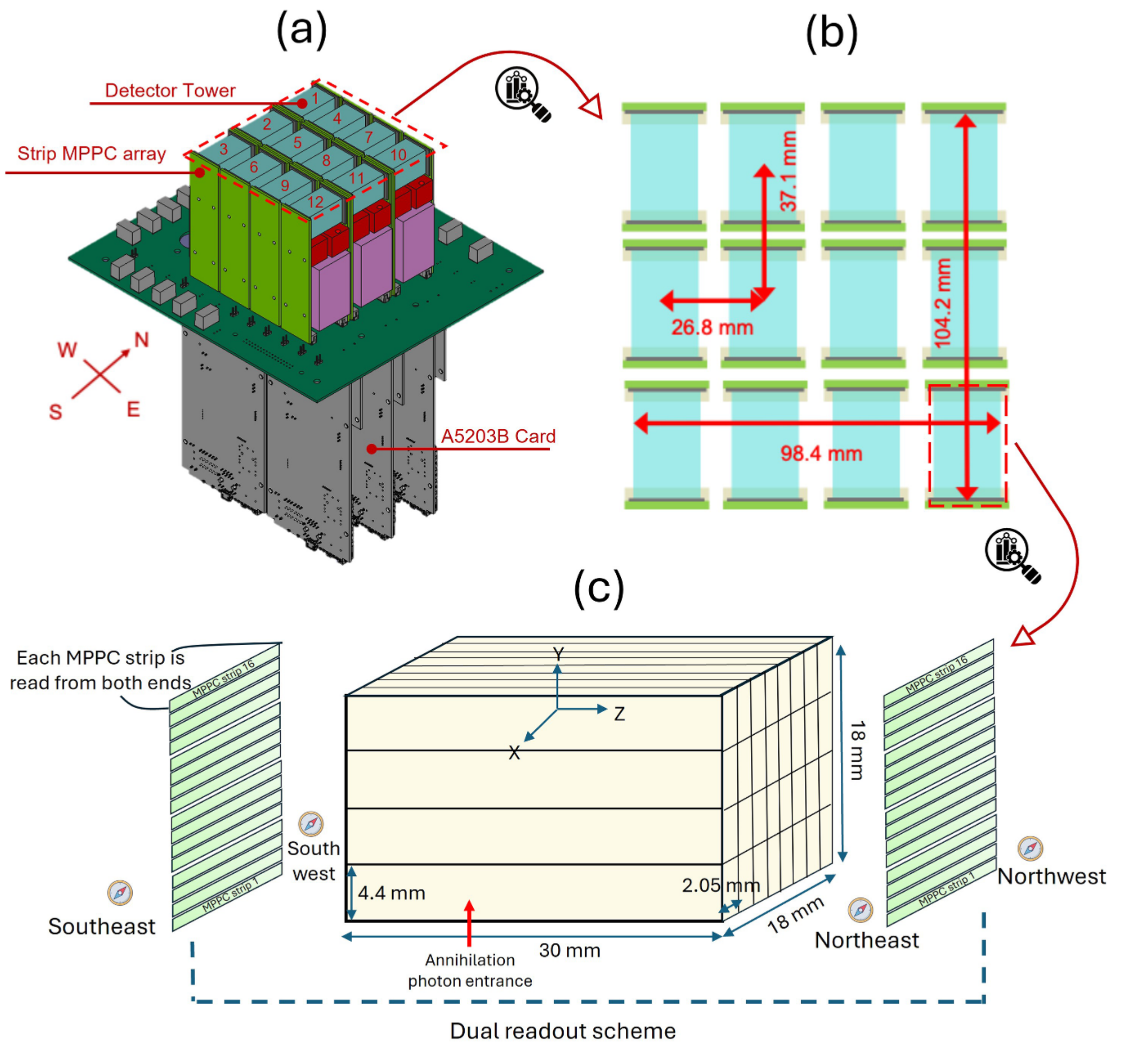

Figure 2. (a) Schematic illustration of the detector panel showing the arrangement of detector towers and the integrated readout electronics. (b) Layout of the 4×3 grid of detector towers on the panel, with center-to-center distances indicated. (c) Illustration of a single four-layer, dual-readout detector tower, highlighting the four directional readout groups (Northeast, Northwest, Southeast, and Southwest).

and time over threshold (ToT) measurements over 128 channels. A full detector panel requires 768 channels; therefore, it is readout with 6 A5203B cards.

A concentrator board works as bridge and synchronization module for all channels, providing data readout, synchronization between the units and broadcasting of commands (e.g. triggers, time resets, etc.). This is carried out using Janus, an open-source software platform tailored for such modular systems. In Janus, each event is encoded as a 32-bit data word (for each channel). The lowest 8 bits contain the ToT information, with a least significant bit (LSB) corresponding to 1.6 ns. The following 19 bits encode the ToA, with a LSB of 3.125 ps. Consequently, the ToA measurement rolls over after $2^{19} \times 3.125 = 1.64\ \mu$s which necessitates the introduction of a frame counter. The timing resolution can reach approximately 7 ps root mean squared (RMS) under stable input amplitude, and around 20 ps RMS when input signal amplitudes vary (Venturini *et al* 2024).

Spontaneous firing of SPADs can cause dark counts and noise in the output signal. To suppress these dark counts, an acceptance threshold was applied on the ToT values whether to record the SMPPC hit or to suppress it. This threshold was set far enough from the 511 keV photopeak to ensure full efficiency. Furthermore, ToT-based corrections are applied in software to compensate for amplitude-dependent timing shifts (walk effect), thus removing the need for hardware-based constant fraction discriminators (Venturini *et al* 2024).

The following section explains how the ToT and ToA values are used to infer the energy deposition, timestamp, and spatial coordinates of the incident annihilation photon.

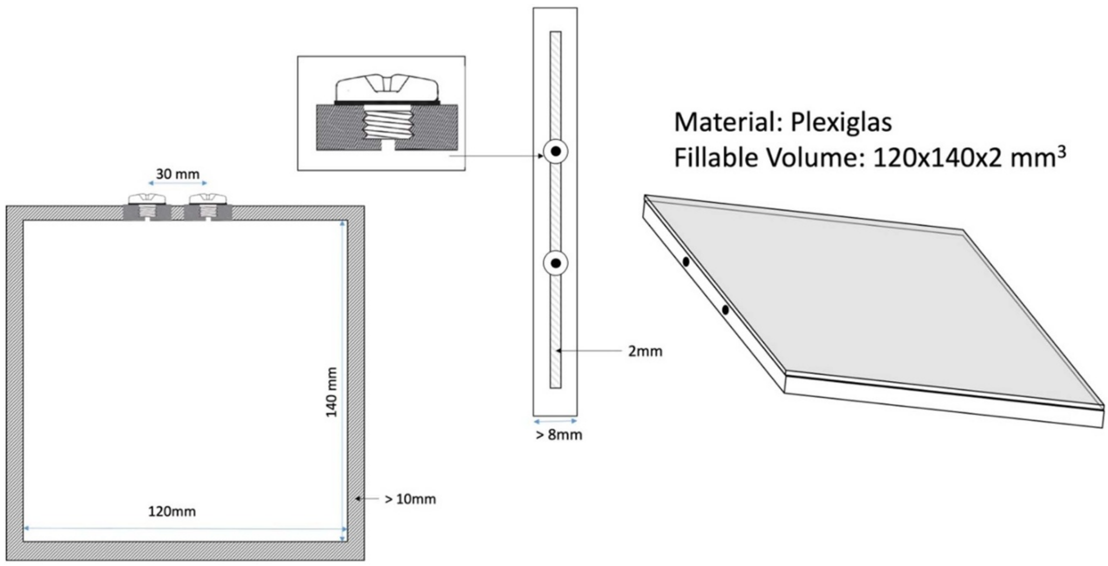

Figure 3. Schematic of the flood illumination phantom used for calibrating the detector panel. The phantom consists of two plexiglass plates enclosing a 2 mm thick fillable cavity, uniformly irradiating the detector surface when filled with ^{18}F.

2.3. Calibration

A flood illumination phantom was constructed using two plexiglass plates sealed together, forming a fillable cavity with 2 mm thickness. A schematic of the phantom is shown in figure 3. The phantom was filled with ^{18}F-FDG to uniformly irradiate the detector panel. For the TOF measurements, the same phantom was positioned midway between the two detector panels, separated by a distance of 30 cm. The activity rate during data acquisition was below the saturation point of the setup to avoid the effects of deadtime. Data acquired from these scans were used for detector calibration.

Layer detection (DOI): Event reconstruction begins with identifying the layer in which the interaction occurred. This is defined as the layer where all its 16 channels register a signal (non-zero ToT). The DOI is then assigned to the geometric center of the identified layer. If, within a single time frame (1.64 μs), more than one layer satisfies this activation condition, each would go through further processing as an independent event: In cases of inter-layer scattering, the events would typically get rejected by the energy window due to insufficient deposited energy; Conversely, if the multi-layer activation is due to arrival of more than one annihilation photon during the time frame, each layer whose energy falls within the 511 keV energy window, will be recorded as a separate event.

Time: Differences in cable lengths and PCB trace lengths among the SMPPC-ASIC channels introduce relative timing offsets. These offsets were corrected among the four channels within each directional group (i.e. NE, NW, SE, SW) of a detector layer. For this purpose, the Gaussian mean of the ToA difference between each channel and the average ToA of its directional group was calculated and applied as a constant correction factor.

After aligning channels' timing within each directional group, a single ToA value was computed to represent that group. It is given in equation (1),

$$\mathrm{ToA}_{\mathrm{Dir}} = \frac{1}{2.7}\left(\mathrm{ToA}_{\mathrm{Dir},1} + 0.8\,\mathrm{ToA}_{\mathrm{Dir},2} + 0.6\,\mathrm{ToA}_{\mathrm{Dir},3} + 0.3\,\mathrm{ToA}_{\mathrm{Dir},4}\right) \tag{1}$$

with Dir indicating the directional group (NE, NW, SE, or SW) and the indices 1-4 referring to the detection times sorted in ascending order. The higher weights assigned to earlier channels reflect the statistical nature of photon arrival times, which approximately follow a Poisson distribution in which the variance equals the mean. Under this model, earlier photon detections carry lower temporal uncertainty, justifying their preferential weighting. The weighting coefficients were determined experimentally and yielded a marginal improvement in CTR. The final event timestamp (t) was then determined as the average of the four directional group ToAs (equation (2)),

$$t = \frac{1}{4}\sum_{\mathrm{Dir}} \mathrm{ToA}_{\mathrm{Dir}}. \tag{2}$$

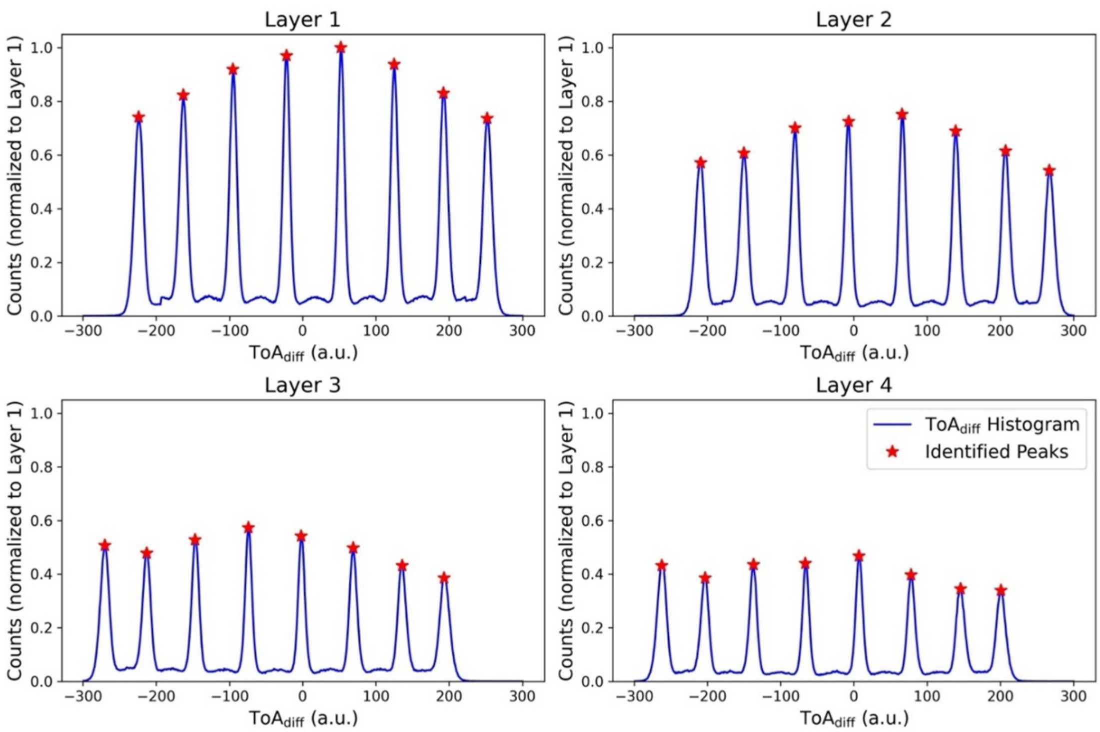

Figure 4. Histogram of the ToA$_{\mathrm{diff}}$ values (used for X-positioning) for layers 1–4 obtained from the flood irradiation. The stars show the identified peaks corresponding to the center of the crystals.

To calibrate the TOF, timing offsets were calculated at the layer-to-layer level for each corresponding detector tower pair. A Gaussian function was fitted to the distribution of coincidence time differences, and the mean used to correct the TOF offset. Importantly, TOF offsets were computed after applying the energy window (as described in the energy calibration section) on events to minimize time walk effects.

X-position: The X-position of the event (crystal identification) is estimated using the difference of ToA values (ToA$_{\mathrm{diff}}$) between East and West side of the layer, i.e. opposite sides of the SMPPCs (equation (3)). This is performed using directional ToA values (ToA$_{\mathrm{Dir}}$) calculated in equation (1),

$$\mathrm{ToA}_{\mathrm{diff}} = \frac{1}{2}\left(\sum_{\mathrm{Dir}\,=\,\mathrm{NE,SE}} \mathrm{ToA}_{\mathrm{Dir}} - \sum_{\mathrm{Dir=NW,SW}} \mathrm{ToA}_{\mathrm{Dir}}\right). \tag{3}$$

A layer specific look-up-table (LUT) was extracted to map the ToA$_{\mathrm{diff}}$ values to *the* X-positions. As shown in figure 4, ToA$_{\mathrm{diff}}$ histograms were calculated separately for each layer. Eight peaks are visible in the histogram which corresponds to the center of the 8 crystals in each layer. A peak detection algorithm identified the peaks. The LUTs were calculated to map the ToA$_{\mathrm{diff}}$ value to X-positions while aligning the peaks (ToA$_{\mathrm{diff}}$ value) with the known crystal-center positions (physical X-coordinates). Based on the resulting X-positions, events in each crystal were grouped to enable further crystal-specific calibration.

Energy: The deposited energy of events is estimated using the average of the 16 ToT values form the SMPPC-ASIC channels reading the corresponding layer (equation (4)),

$$\mathrm{ToT}_{\mathrm{mean}} = \frac{1}{16}\sum_{\mathrm{Dir=NE,NW,SE,SW}}\sum_{i=1}^{4}\mathrm{ToT}_{\mathrm{Dir},i}. \tag{4}$$

Energy calibration was performed at the crystal level. Using the flood data, the ToT$_{\mathrm{mean}}$ histogram was calculated for each crystal, and a peak detection algorithm identified the peak corresponding to the 511 keV photopeak. A Gaussian function was fitted to the peak, and the full width at tenth maximum (FWTM) window was used as the accepting energy window for each crystal.

Z-Position: Two sources of information were used for Z-position estimation. Due to the attenuation of scintillation light as it propagates along the crystal length, an inverse relationship exists between the signal amplitude (ToT value) recorded by SMPPCs and their distance from the interaction point of the incident annihilation photon. This provides the first source of information, defined as the difference in ToT values measured at the North and South ends of the crystal. This difference, denoted as $\mathrm{ToT_{diff}}$, was calculated by subtracting the average ToT value of the North side (averaged across the eight corresponding channels) from that of the South side (equation (5)),

$$\mathrm{ToT_{diff}} = \frac{1}{8}\left(\sum_{\mathrm{Dir=NE,NW}}\sum_{i=1}^{4}\mathrm{ToT}_{Dir,i} - \sum_{\mathrm{Dir=SE,SW}}\sum_{i=1}^{4}\mathrm{ToT}_{\mathrm{Dir},i}\right). \tag{5}$$

However, the relationship between the ToT value and the event-to-SMPPC distance breaks down at short distances due to saturation of the SMPPCs. This effect is illustrated in figure 5(a), which shows the $\mathrm{ToT_{diff}}$ histogram for events in a single crystal obtained from the flood illumination data. Under uniform irradiation, a uniform histogram would be expected. Instead, the histogram exhibits sharp peaks at both extremes, indicating reduced responsiveness of $\mathrm{ToT_{diff}}$ to changes in interaction position near the crystal ends. This diminished positional responsiveness leads to degraded spatial resolution in these regions.

To mitigate this limitation, a second source of information was introduced for Z-position estimation. When scintillation light reaches the interface between the crystal ($n = 1.82$) and the crystal-SMPPC coupling epoxy glue layer ($n = 1.53$), part of it is reflected back into the crystal because of the refractive index mismatch. Photons striking the interface at angles larger than the critical angle are totally internally reflected rather than transmitted toward the SMPPC array (figure 5(b)). This effect becomes significant when an interaction occurs near the crystal end. As shown in figure 5(b) this will cause the four SMPPCs to receive unequal numbers of scintillation photons and therefore record different ToT values. The magnitude of this inequality increases progressively as the interaction point approaches the crystal end.

This information was utilized as the difference between the maximum and minimum ToT values among the four SMPPCs located at North (denoted as $\mathrm{ToT_{N\_range}}$) or South (denoted as $\mathrm{ToT_{S\_range}}$) end of the crystal (equation (6)),

$$\mathrm{ToT_{N\_range}} = \mathrm{ToT_{N,4}} - \mathrm{ToT_{N,1}}. \tag{6}$$

With $\mathrm{ToT}_{\mathrm{N},i} = \frac{1}{2}\left(\mathrm{ToT}_{\mathrm{NE},i} + \mathrm{ToT}_{\mathrm{NW},i}\right)$, and $i = 1$ (minimum ToT) or 4 (maximum ToT). $\mathrm{ToT_{S\_range}}$ was computed analogously.

However, $\mathrm{ToT_{N\_range}}$ and $\mathrm{ToT}_{S\_\mathrm{range}}$ are only informative for events occurring near the crystal ends. When the interaction point is located farther from the ends, the scintillation light is more uniformly distributed across the four SMPPCs, and variations in their ToT values arise mainly from statistical fluctuations rather than spatial dependence on the interaction point. This is better shown in figure 5(c), which presents $\mathrm{ToT_{diff}}$ plotted against ($\mathrm{ToT_{N\_range}}$ —$\mathrm{ToT_{S\_range}}$). At the extremes of $\mathrm{ToT_{diff}}$, representing interactions near the North and South crystal ends, the absolute value of ($\mathrm{ToT_{N\_range}}$ —$\mathrm{ToT_{S\_range}}$) increases, indicating elevated $\mathrm{ToT_{N\_range}}$ near the North side and $\mathrm{ToT_{S\_range}}$ near the South side. In contrast, for events occurring away from the crystal edges, ($\mathrm{ToT_{N\_range}}$ —$\mathrm{ToT_{S\_range}}$) shows no positional trend, confirming that it is not sensitive to depth for interactions away from crystal ends.

Hence, before utilizing $\mathrm{ToT_{N\_range}}$ and $\mathrm{ToT_{S\_range}}$, we aimed to neutralize them for events away from the crystal ends. Figure 5(d) shows the $\mathrm{ToT_{N\_range}}$ histogram for events in a crystal obtained from flood-illumination data. The distribution is approximately Gaussian, with an extended tail. The tail corresponds to interactions near the North end of the crystal, while the main body of the distribution corresponds to events occurring elsewhere in the crystal, where differences in $\mathrm{ToT_{N\_range}}$ are primarily statistical. To isolate the tail, a Gaussian mixture model (GMM) was fitted to the distributions as shown on the plot in figure 5(d). The intersection point of the two components of the GMM fit (denoted as α) was used as a threshold on the $\mathrm{ToT_{N\_range}}$, activating it only for events close to the North end of crystal (equation (7)):

$$\mathrm{ToT}_{N\_\mathrm{range}} = \left(\mathrm{ToT}_{N\_\mathrm{range}} - \alpha\right)/2. \tag{7}$$

While the negative values are set to zero, and it is scaled by a factor of 2 to match the dynamic range of $\mathrm{ToT_{diff}}$ prior to combination. Same procedure was applied to the $\mathrm{ToT_{S\_range}}$.

Eventually, as shown in equation (8), the two sources of information were combined into a single variable, denoted as $\mathrm{ToT_{comb}}$. Due to the thresholds applied on the $\mathrm{ToT_{N\_range}}$ and $\mathrm{ToT_{S\_range}}$ (equation (7)), the $\mathrm{ToT_{comb}}$ will be reduced to $\mathrm{ToT_{diff}}$ for events away from both ends; will be equal to $\mathrm{ToT_{diff}} + \mathrm{ToT}_{N\_\mathrm{range}}$ for events at the North end; and equal to $\mathrm{ToT_{diff}} - \mathrm{ToT_{S\_range}}$ for events at the South

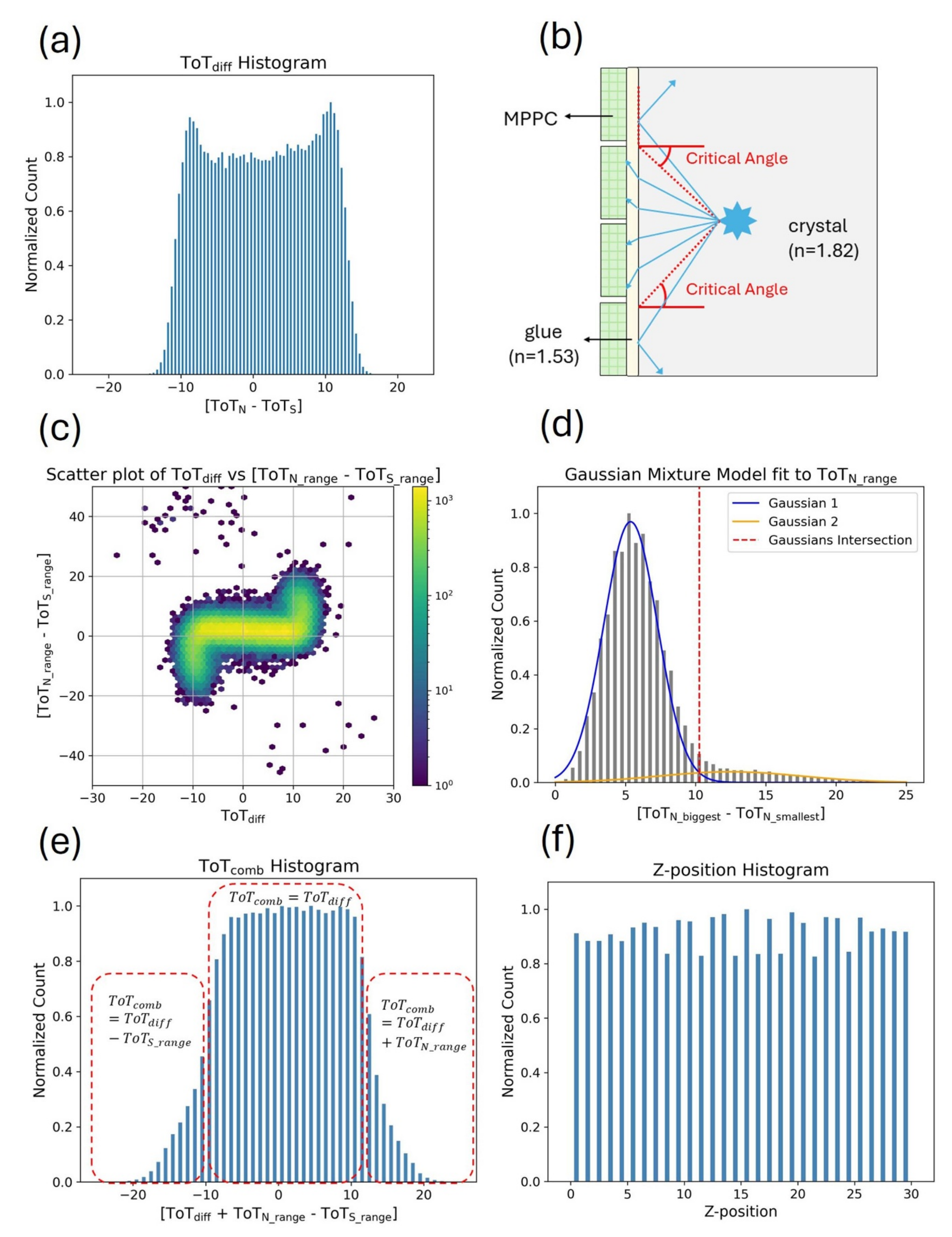

Figure 5. (a) Histogram of ToT_{diff} for events in a single crystal obtained from flood irradiation data. Sharp peaks are evident at both extremes, indicating reduced spatial responsiveness of ToT_{diff} for interactions occurring near the crystal ends. (b) Schematic illustration of the total internal reflection at the crystal-SMPPC interface. Photons emitted from an event close to crystal end and incident at angles larger than the critical angle are reflected back into the crystal rather than transmitted toward the SMPPC array. This leads to uneven light distribution across the four SMPPCs. (c) ToT_{diff} plotted against the [ToT_{N_range}—ToT_{S_range}]. At the extremes of ToT_{diff}, corresponding to events at the crystal ends, the absolute value of [ToT_{N_range} —ToT_{S_range}] increases, while away from crystal ends, no trend is visible. (d) Histogram of ToT_{N_range}. The fitted Gaussian mixture model to distinguish between events occurring near the North side (tail) and rest of events (main body), is shown on the plot. (e) Histogram of the ToT_{comb}. The dynamic range of the signal is increased at the ends of the crystal. The regions shown with dashed lines are approximate. (f) the histogram of the Z-positions mapped from ToT_{comb} using the calibration LUT.

end. Thus, the dynamic range of ToT_{comb} is effectively increased at the ends of the crystal compared to ToT_{diff} alone. Figure 5(e) shows the histogram of ToT_{comb} for events in a crystal under flood uniform irradiation. As shown, the dynamic range of the signal is increased at the ends of the crystal,

$$\mathrm{ToT_{comb}} = \mathrm{ToT_{diff}} + \mathrm{ToT}_{N\_\mathrm{range}} - \mathrm{ToT}_{S\_\mathrm{range}}. \tag{8}$$

The next step included mapping the $\mathrm{ToT_{comb}}$ values to Z-positions. The objective was to divide the $\mathrm{ToT_{comb}}$ range into segments, with each segment corresponding to a specific Z-position along the crystal's length. Assuming uniform irradiation from the flood phantom, if each segment contains an equal number of events, the segments can be associated with equally spaced physical positions along the crystal. Accordingly, the $\mathrm{ToT_{comb}}$ values from the calibration data were partitioned so that all segments contained an equal number of events. The boundaries of these segments were then used to construct a LUT that maps $\mathrm{ToT_{comb}}$ values to physical Z-positions. Figure 5(f) shows the histogram of the Z-positions (mapped using the calibration LUT) for events in a crystal under uniform irradiation. As expected, the distribution of events across segments is approximately uniform.

2.4. Evaluation

An additional flood illumination data was acquired to evaluate the detectors' performance. This acquisition was performed at a different time throughout the day, with the detectors being restarted between sessions to assess the stability of the system under varying temperature conditions and repeated power cycles. In addition, a radiolucent carbon fiber bed was placed between the detector panel and the flood irradiation source to account for the scattering impact of the bed. Key performance metrics including energy resolution, and CTR were measured, and the stability of the detectors across acquisitions was assessed.

To report the energy resolution, we performed a full spectrum energy calibration on one detector. The $\mathrm{ToT_{mean}}$ is a non-linear function of the interactions' deposited energy and must be corrected before accurate energy resolution calculation. To this end, we irradiated a detector tower with various isotopes having different gamma peaks. The isotopes and their photopeak energies included: ^{131}I (364 keV), ^{22}Na (511 keV and 1274 keV), and ^{137}Cs (662 keV) and the intrinsic gamma peaks from ^{176}Lu present in the LFS crystals, at 202 keV and 307 keV. A 3rd order polynomial function was fitted to the photopeak positions and their corresponding ToT values for each crystal in the detector tower. The result was then applied to the flood irradiation data to extract corrected energy spectrum and calculate the energy resolution. A Gaussian function was fitted on the 511 keV photopeak, and energy resolution was calculated as the full-width-half-maximum (FWHM) of the Gaussian divided by the photopeak.

An additional experiment was conducted to evaluate the detector's Z-positioning performance. One of the detector towers was irradiated using a sub-millimeter slit positioned at multiple locations along the 30 mm length of the crystals. The slit was formed by two laterally arranged lead blocks, with a syringe containing ^{18}F placed on top as the radiation source. Measurements were taken at 19 discrete positions. The slit was placed on top of a radiolucent carbon-fiber bed (7 mm thickness) with the detector underneath affixed to a motorized translation motor capable of 0.1 mm positioning accuracy. The total distance from the slit to the detector surface was 22 mm. The acquired data were used to assess both the linearity and spatial resolution of the detector's Z-positioning capability. For each step, a Gaussian function was fitted to the resulting Z-positions distribution, with the mean value representing the estimated Z-position and the FWHM reported as the spatial resolution.

3. Results

A total of 2.6 million coincidence events were recorded during the test flood data acquisition after applying both energy and coincidence time window constraints. The energy window was defined individually for each crystal and corresponded to the FWTM of the 511 keV photopeak. A coincidence time window of $\pm$250 ps was applied. Table 1 summarizes the normalized number of coincidence events detected for each detector layer pair, with all counts normalized to those recorded between layer 1–layer 1.

3.1. Time

To evaluate whether the timing offsets between the 4 SMPPC-ASIC channels in each directional group is constant across acquisitions, the offsets were calculated using the test flood data and compared to the ones calculated using the calibration data. The offset difference was below 1 ps across the whole panel, showing the constant nature of the offsets. Supplementary figure S1 presents heatmaps showing the variation of the offsets, for one example detector tower.

The CTR was calculated at the layer-to-layer level for each corresponding detector tower pair and reported as the FWHM of a Gaussian function fitted to the distribution of coincidence time differences. Supplementary figure S2 presents the coincidence time distributions and corresponding Gaussian fits for all layer pairs between two corresponding detector towers. Figure 6 presents heatmaps showing the

Table 1. Normalized number of coincidence events in each layer pair in the flood data.

	Layer 1	Layer 2	Layer 3	Layer 4
Layer 1	1	0.77	0.59	0.45
Layer 2	0.77	0.59	0.46	0.35
Layer 3	0.59	0.45	0.35	0.28
Layer 4	0.45	0.35	0.27	0.22

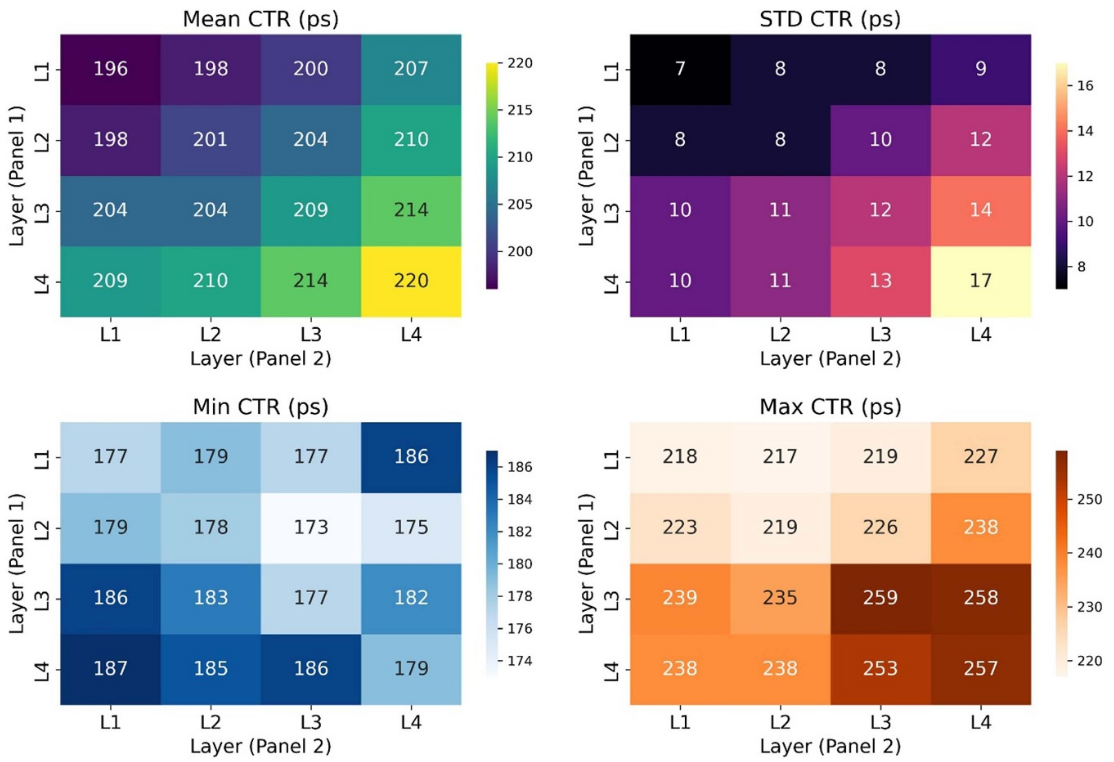

Figure 6. Heatmaps showing the mean, standard deviation (std), minimum (Min), and maximum (Max) of CTR for each pair of layers on two detector panels. Each cell in the heatmaps corresponds to a specific layer pair, representing the respective parameter computed from 144 CTR measurements, one for each pair of detector towers (12 towers per panel, resulting in $12 \times 12 = 144$ combinations).

mean, standard deviation (std), minimum, and maximum CTR for each pair of detector layers across the two panels. Each cell in the heatmaps corresponds to a specific layer pair and represents the respective parameter (mean, std, min, and max) computed from 144 CTR measurements. Each measurement corresponds to one combination of detector towers, with 12 towers per panel, resulting in $12 \times 12 = 144$ total pairs. The CTR (average FWHM $\pm$ std) was 196 $\pm$ 7 ps for layer 1 vs. layer 1, and it gradually degraded for higher layer to layer pairs reaching 220 $\pm$ 17 ps for layer 4 vs. layer 4 pair. The best and worst obtained CTRs were 173 ps and 259 ps, respectively.

Table 2 shows the results of the TOF measurement stability. This was obtained by measuring the error in calculating the TOF between the calibration and the test flood data. The mean absolute error (MeanAE) and maximum absolute error (MaxAE) for each layer pair is reported. Similar to the heatmaps in figure 6, each cell represents parameters computed from 144 error measurements. The MeanAE was 3 ps for layer 1 vs layer 1 and degraded to 6 ps for layer 4 vs layer 4. The MaxAEs of 9 ps and 22 ps were obtained for layer 1 vs layer 1 and layer 4 vs layer 4, respectively.

3.2. X-positioning

Figure 7 shows the calibrated X-positions of events from the test flood data for Layers 1 through 4 in a representative detector tower. Eight distinct peaks are visible in each layer, corresponding to the centers of the eight individual crystals. The vertical lines show the known physical position of the crystal centers, which is perfectly aligned with the peaks after calibration. To evaluate the linearity of the X-positioning after calibration, the peak positions were extracted and compared to the known physical centers of the

Table 2. Mean and maximum absolute error in calculation of layer-to-layer TOF between calibration and test flood data. Each cell represents respective parameters computed from 144 instances of the layer pair from 12 tower on each panel.

	Mean absolute error (ps)				Maximum absolute error (ps)			
	L1	L2	L3	L4	L1	L2	L3	L4
L1	3	3	4	4	9	12	16	16
L2	3	4	4	5	13	15	14	18
L3	4	4	5	6	15	15	20	24
L4	5	5	5	6	15	15	17	22

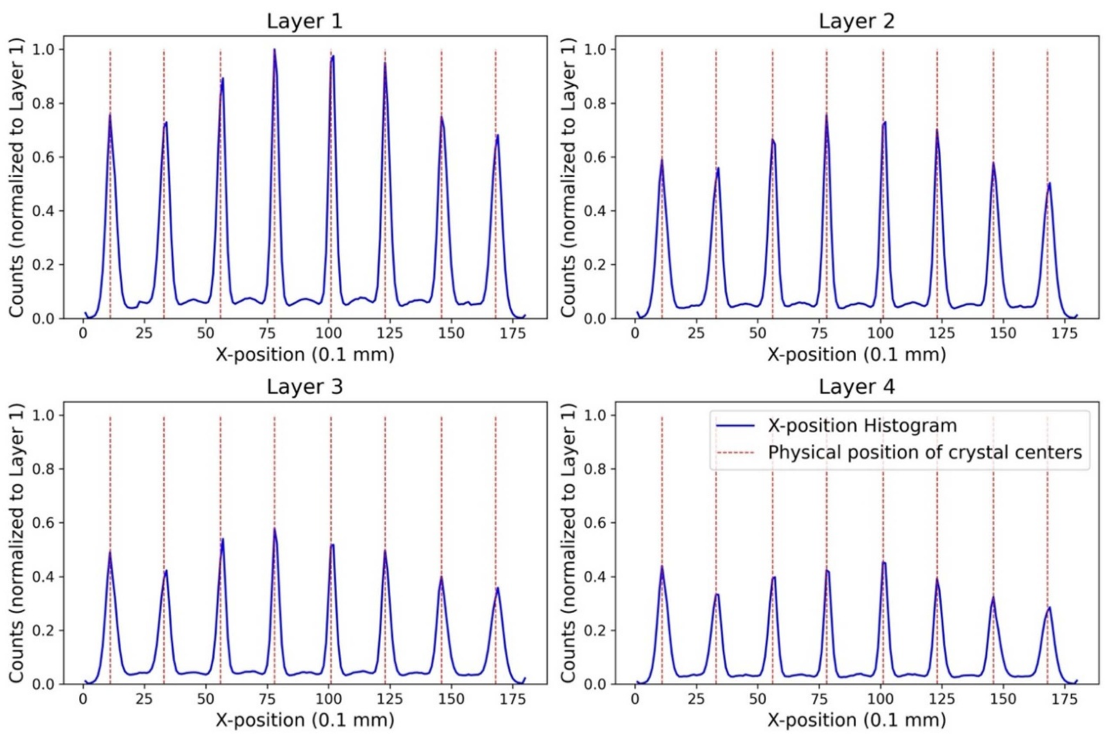

Figure 7. Calibrated X-positions of events from the test flood data for layers 1 through 4 in a representative detector tower. Peaks corresponding to the centers of the eight individual crystals perfectly match the vertical lines showing the known physical position of the crystal centers.

corresponding crystals. The absolute error between the measured and expected positions was computed for each crystal.

Table 3 summarizes the MeanAE and MaxAE of the X-positions of the crystal centers. These metrics were computed across all 12 detector towers on a detector panel. For example, the MeanAE reported for crystal 5 in layer 1 represents the average over the 12 instances of that crystal (i.e. Crystal 5, layer 1) across the 12 towers. As indicated in the table, MeanAE and MaxAE were below 0.1 mm for all the crystals, indicating excellent linearity in X-positioning. Similar tables can be generated for individual detector towers for in-detail analysis in routine recalibration and performance monitoring.

3.3. Energy

Using multiple photopeaks from various gamma emitters, a crystal-specific polynomial calibration function was derived to convert ToT_{mean} values to energy in keV for each crystal in a representative detector tower. Figure 8 illustrates the calibration procedure for one representative crystal: panel (a) shows the non-calibrated energy spectrum in terms of ToT_{mean}, panel (b) displays the fitted polynomial function mapping ToT_{mean} to the keV domain, and panel (c) presents the resulting calibrated energy spectrum.

Using the extracted polynomial functions, ToT_{mean} values from the test flood data were converted to a linearized energy scale in keV. Energy resolution was then calculated for each crystal in the tower, defined as the percentage FWHM over the 511 keV photopeak. Table 4 summarizes the energy resolution values for all crystals. The individual crystal resolutions ranged from 13% to 16%. The average energy resolutions for crystals in layers 1 through 4 were 14.2% ± 0.8, 14.3% ± 0.8, 15.3% ± 1.0, and

Table 3. Mean and maximum absolute error in X-positioning of the known crystal centers. These metrics were computed across all 12 detector towers on a detector panel. For example, the MeanAE reported for crystal 5 in layer 1 represents the average over the 12 instances of that crystal (i.e. Crystal 5, layer 1) across the 12 towers.

	Mean absolute error (mm)				Maximum absolute error (mm)			
	L1	L2	L3	L4	L1	L2	L3	L4
C1	0	0	0	0	0	0	0	0
C2	0	0	0	0	0.1	0	0.1	0
C3	0	0	0	0	0	0.1	0.1	0.1
C4	0	0	0	0	0	0	0.1	0
C5	0	0	0	0	0.1	0.1	0.1	0.1
C6	0	0	0	0	0	0.1	0.1	0.1
C7	0	0	0	0	0.1	0.1	0.1	0.1
C8	0.1	0	0	0	0.1	0.1	0.1	0.1

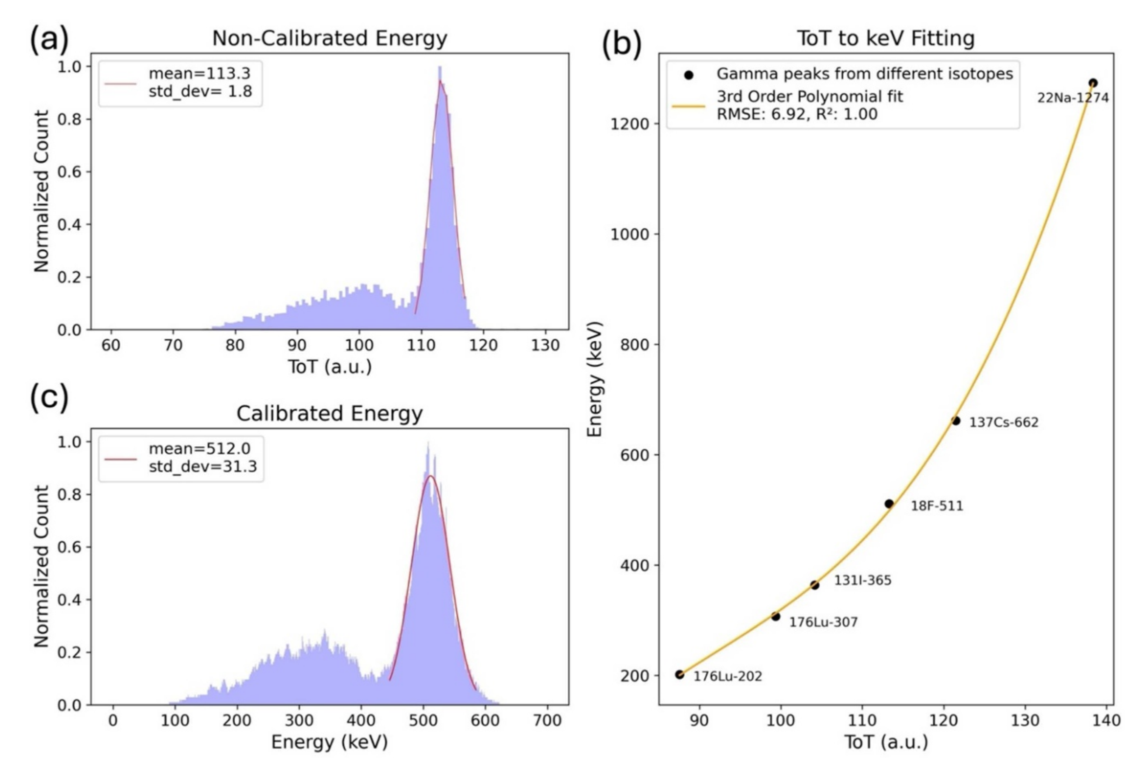

Figure 8. (a) Non-calibrated energy spectrum of a crystal under flood irradiation. The 511 keV photopeak is perfectly visible and can be isolated. (b) The polynomial fit between the ToT range and the deposited energy of the event in keV unit. (c) Calibrated energy spectrum of the same crystal.

Table 4. The energy resolution over the 511 keV photopeak, measured for each crystal in a detector tower. The columns are crystals, and the rows are the layers. Values are in percentage.

%	C1	C2	C3	C4	C5	C6	C7	C8	Average
L1	13.4	13.2	14.9	15.1	14.2	15.2	14.2	13.5	14.2 ± 0.8
L2	14.3	14.8	15.9	13.6	14.1	14.5	13.1	14.1	14.3 ± 0.8
L3	14.3	15.1	16.8	16.2	14.7	15.8	14.0	15.2	15.3 ± 1
L4	13.6	14.9	15.6	16.2	15.8	14.5	16.6	16.0	15.4 ± 1

15.4% $\pm$ 1.0, respectively. Supplementary figure S3 shows the calibrated energy spectra for all crystals in the detector tower.

To evaluate the stability of the detector in energy identification, we calculated the error of the 511 keV photopeak between two flood acquisitions. Table 5 reports the MeanAE and MaxAE across all crystals. These statistics were computed over the 12 detector towers on a single panel. The MeanAE and MaxAE were found to be below 1.2 keV and 6 keV, respectively, indicating good stability. For detailed performance monitoring, individual tables can be generated to report errors separately for each detector tower.

Table 5. Mean and maximum absolute error in calculation of 511 keV photopeak between calibration and test data. These parameters were computed over the 12 detector towers on a panel.

	Mean absolute error (keV)				Maximum absolute error (keV)			
	L1	L2	L3	L4	L1	L2	L3	L4
C1	0.4	0.5	0.7	0.6	1	2	4	4
C2	0.6	1	0.3	0.7	1.9	4	2	3
C3	0.6	0.3	0.8	0.8	1.7	1.1	3	2.8
C4	0.7	0.6	0.4	0.8	3	3	2	4
C5	0.9	0.6	0.3	1.2	3	2	1	6
C6	0.7	0.6	0.8	0.9	3	2	3	3
C7	0.8	0.4	1.1	0.5	3	1.3	4	3
C8	0.5	0.9	0.5	0.5	1	2.4	2	3

3.4. Z-positioning

The Z-position was calculated using $\mathrm{ToT_{comb}}$ (equation (8)), a composite parameter which integrates two complementary sources of information, including the signal-amplitude difference between the crystal ends ($\mathrm{ToT_{diff}}$, equation (5) and the signal-amplitude range on each end ($\mathrm{ToT_{N\_range}}$ and $\mathrm{ToT_{S\_range}}$ (equations (6) and (7)). Assuming uniform irradiation with the flood phantom, a crystal-specific LUT was then generated to map $\mathrm{ToT_{comb}}$ values to Z-positions, ensuring a uniform distribution of events along the crystal's length. To quantitatively evaluate the post-calibration uniformity of Z-positions under flood illumination, each crystal was divided into 30 segments (1 mm each), and the average event count per segment was calculated. For every segment, the percentage error relative to the crystal's mean count was computed as the absolute difference between the segment count and the mean count, divided by the mean count.

Figure 9 presents heatmaps of the mean percentage error for each 1 mm Z-segment across all 12 detector towers. Each cell in the heatmap represents the average percentage error of a specific Z-segment across its 12 instances (e.g. segment 5, crystal 5, layer 1 across all 12 towers). As shown, the average bin-wise percentage error remained below 8%, indicating good uniformity of counts in each segment, under the LUT-based Z-position calibration. Similar heatmaps can also be generated on a per-tower basis to validate the mapping performance at the individual detector level.

Figure 10 summarizes the results of the slit irradiation test. Panel (a) shows a schematic of the setup used to irradiate the detector tower with a sub-millimeter slit. Panel (b) presents the linearity of the detector's response. Across 19 discrete irradiation points along the crystal's length, the measured positions showed excellent agreement with the ground truth, with a MeanAE of 0.26, 0.24, 0.21, 0.24 mm for layer 1 through 4, respectively. Panel (c) shows the Gaussian fits on the distribution of Z-positions for all the 19 measurement steps for layer 1. Panel (d) displays the Z-positioning resolution per layer, for all the 19 steps. For layer 1 through 4, an average FWHM of 3.78, 3.84, 4.01, and 4.78 mm was obtained across the 19 slit positions. Supplementary figure S4 shows the distribution of Z-positions under slit measurement for 4 of the steps with their corresponding Gaussian fit.

4. Discussion

In this study, we developed a PET detector panel comprising four-layered dual-readout DOI-TOF detector towers, specifically designed for integration into organ- or purpose-dedicated PET scanners. The panel is designed as a fully integrated, ready-to-use module, incorporating a high-performance compact electronics system based on the picoTDC ASIC.

A central innovation of our design lies in the use of SMPPC arrays read out from both ends using two independent electronic channels. In this configuration, each detector layer is coupled to 8 SMPPCs, four per side, resulting in each scintillation event being detected by 8 SMPPCs and read out via 16 electronic channels. This high degree of signal redundancy enhances measurement precision by reducing statistical uncertainty and improving spatial and temporal resolution. Another major methodological contribution of this work is the development of an effortless calibration procedure based on a single uniform flood-irradiation acquisition, which circumvents the need for point-by-point irradiations typically required for the calibration of dual-readout detectors. Finally, detector-level performance evaluation was conducted under realistic operating conditions. Energy resolution and event localization were assessed using a full detector panel comprising 12 towers, while TOF performance was evaluated in coincidence between two complete panels. In addition to performance metrics, we also investigated the operational robustness of the detector by testing its stability under temperature variations and repeated

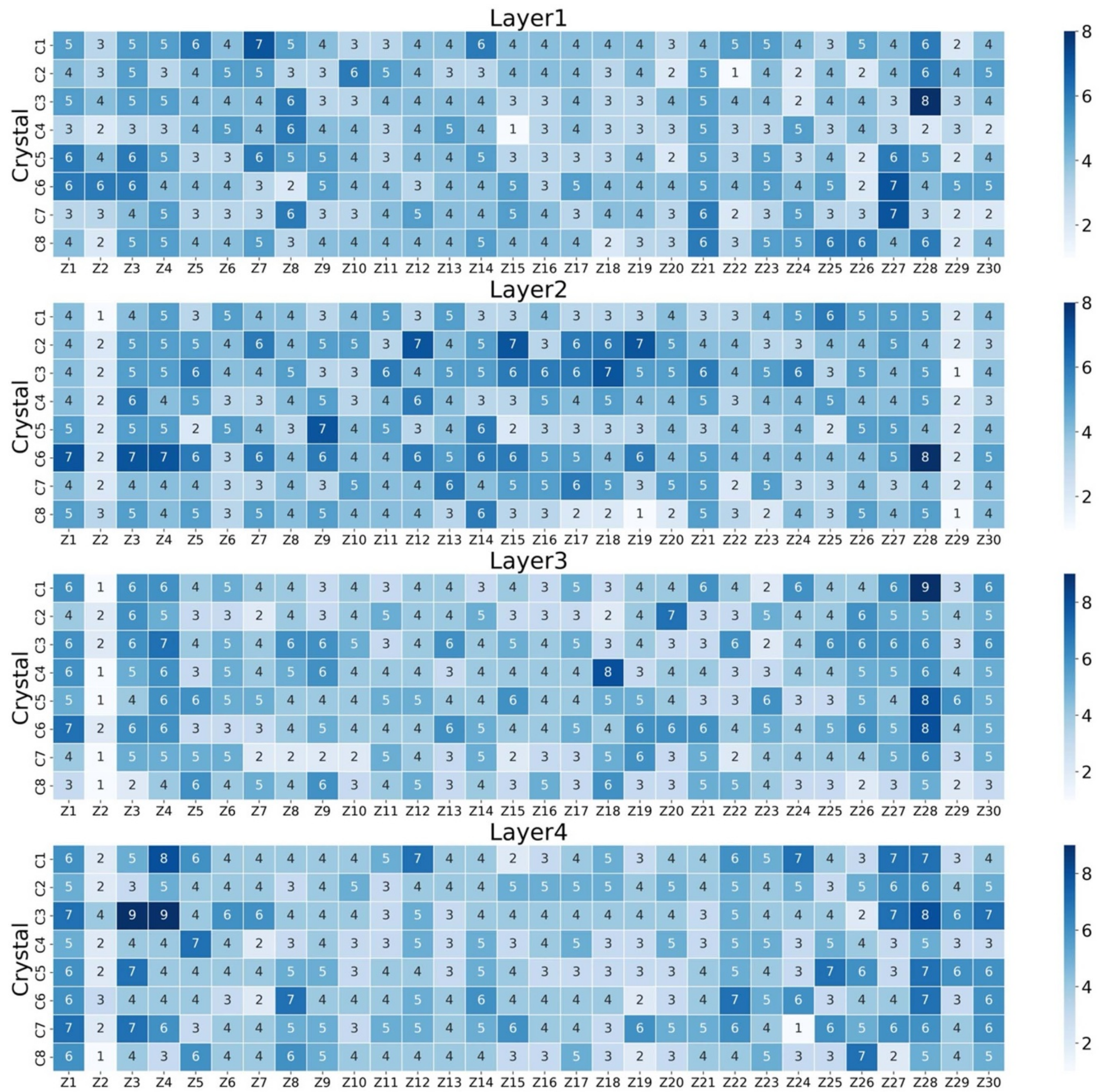

Figure 9. Heatmaps of the mean percentage error for each 1 mm Z-segment, across all 12 detector towers. The percentage error was defined as the absolute difference between the segment's count and the mean count of corresponding crystal, divided by the mean count of crystal. Each cell in the heatmap represents the average percentage error of a specific Z-segment over its 12 instances (e.g. Z-segment 5, crystal 5, layer 1 across all 12 towers).

power cycling. Where appropriate, performance results were reported at the layer and crystal level to ensure a comprehensive and detailed characterization of the detector's capabilities.

4.1. Inter-crystal and inter-layer scatter correction

According to our detector configuration, scattering events within the towers can be categorized as inter-crystal, inter-layer, or a combination of both. Inter-crystal scattering (ICS) refers to events in which a photon scatters between multiple crystals within the same layer but deposits its entire energy (or enough energy to pass the energy window) within that layer. Due to the optical coupling scheme, where each layer's SMPPCs are attached to all eight crystals, and each crystal is coupled to all eight SMPPCs, such ICS events cannot be separated and will be recorded as a single event. In this case, the measured ToT values represent the summed contribution of multiple scattering interactions within the layer. The ToA value, although determined by the arrival time of the first photoelectrons, would as well be affected by the ICS. The scattering interactions occur only a few picoseconds apart, while the subsequent scintillation photons propagate with a reduced velocity due to the refractive index of the crystal. As a result, the recorded ToA will most likely be dominated by the interaction point that is closest to the photosensors.

In contrast, inter-layer scattering can be identified and treated accordingly, as each layer has an independent readout unit. In the current analysis, such events are typically rejected because none of the partial energy depositions across layers satisfy the corresponding energy window. However, dedicated inter-layer scatter recovery methods could identify these events and retain them by correctly assigning

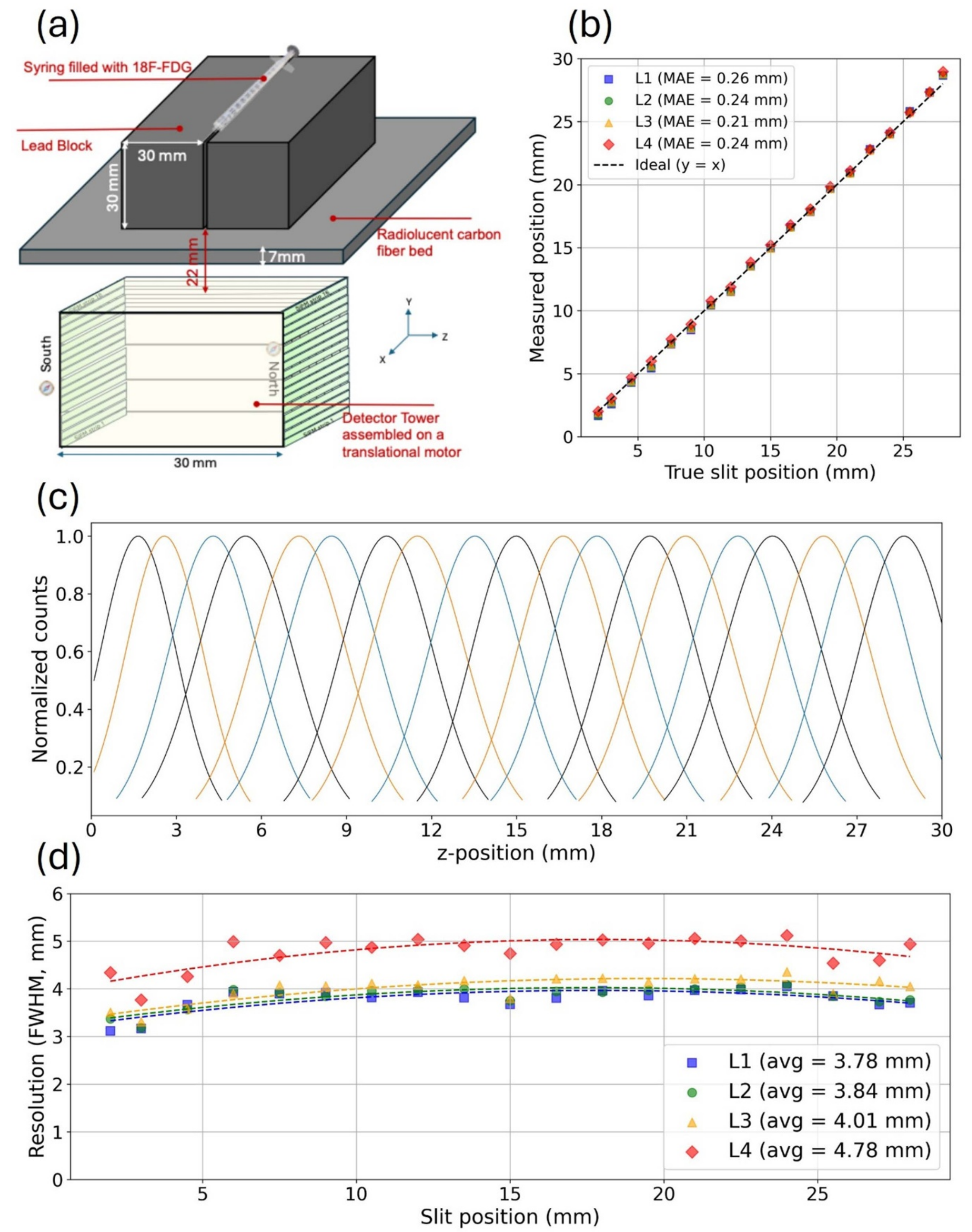

Figure 10. (a) Schematic of the setup used to irradiate the detector tower with a sub-millimeter slit. (b) Presents the linearity of the detector's response by showing where the slit was placed vs where the Z-position appeared. (c) Gaussian fits on the distribution of Z-positions for all the 19 measurement steps for Layer 1. (d) Plots of the Z-positioning resolution (FWHM) for each Layer individually.

the first interaction layer. Preliminary Monte Carlo simulations presented in (Amini *et al* 2024) studied this behavior, but inter-layer scatter correction was not implemented in the present work. One challenge in implementing such correction is the need for full-spectrum energy calibration for energy-based recovery methods, the time-consuming and labor-intensive nature of which is further discussed in the Energy Calibration section. A detailed analysis and implementation of various correction strategies (Lee *et al* 2024) will be investigated in future studies.

4.2. Time

To estimate the event timing, we calculated a weighted average of the ToA values obtained from the four SMPPC-ASIC channels on each directional group. Higher weights were assigned to earlier channels, based on the statistical behavior of photon arrival times, which approximate a Poisson distribution, where the variance equals the mean. Under this model, earlier channels provide more precise estimate of the event's incident time, justifying their preferential weighting. Using this method, we achieved an average CTR of 196 ± 7 ps for layer 1–layer 1 detector pairs, with best value as low as 173 ps (see figure 6). As expected, CTR performance gradually degraded for deeper layer combinations, reaching an average of 220 ± 17 ps for layer 4–layer 4 pairs. This degradation is primarily attributed to a higher fraction of scattered events in deeper layers. Furthermore, lower statistics in deeper layer pairs can marginally contribute to this degradation.

We believe the detector's timing performance can be further enhanced by introducing directionally adaptive weighting, i.e. assigning greater weight to directional groups closer to the estimated interaction location. Another promising avenue is the identification and recovery of inter-layer Compton scatter events, which could reduce scatter contamination and enhance timing resolution. Moreover, in this study, we restricted the analysis to events within the FWTM of the Gaussian fitted to the 511 keV photopeak. Further improvements could be achieved by applying narrower energy windows, which may be especially beneficial for deeper layers where scatter is more prevalent. All these potential enhancements are currently under investigation. However, they fall outside the scope of this study and will be reported in future work focusing specifically on timing performance optimization.

4.3. X-positioning

In conventional crystal arrays (excluding configurations with one-to-one crystal–photodetector coupling), event positioning is typically derived using charge-based center-of-gravity methods, which are susceptible to light compression effects and lead to nonlinear spatial response. In contrast, our approach estimates the X-position from the temporal difference between signals read at the perpendicular ends of the SMPPCs. The $\mathrm{ToA_{diff}}$ is governed by the propagation distance of the signal generated by the first firing SPADs to the readout channels at the ends of the SMPPCs. Naturally, fixed electronic offsets exist between the opposite ends of the SMPPCs, an effect visible in figure 4, as the plots are not symmetric around zero. A simple LUT-based calibration (described in *Methods, C. Calibration, X-positioning*) accurately maps $\mathrm{ToA_{diff}}$ values to X-positions, correcting for the electronic temporal offsets and achieving a linear response. The detector demonstrated excellent X-positioning linearity (figure 7 and table 3), with negligible deviation between the identified X-position peaks and the geometric centers of the corresponding crystals. Furthermore, as shown in figure 7, the inter-crystal valleys in the X-position histogram approached near zero counts, indicating clear discrimination between adjacent crystals.

4.4. Energy

Energy calibration was performed at the crystal level to account for variations in the recorded photopeak position among crystals. In particular, the two lateral crystals at the edges of each detector layer exhibited lower ToT values for the 511 keV photopeak compared to the central crystals. This reduction is attributed to optical light loss at the array boundaries, primarily caused by the refractive index mismatch between the crystal material ($n \approx 1.82$) and the coupling epoxy ($n \approx 1.53$), which leads to scintillation photons refracting away from the SMPPCs at the outer edges of the detector. This effect is illustrated in supplementary figure S5.

To accurately report the energy resolution, we irradiated the detector with multiple radioisotopes with distinct gamma peaks and used it to construct a linearized energy spectrum. Using this approach, we achieved an average energy resolution of 14.2% ± 0.8% for crystals in layer 1, which degraded to 15.4% ± 1.0% in layer 4, a decline primarily due to the increased occurrence of scatter events in deeper regions of the detector. The overall energy resolution obtained with our proposed detector was lower than that typically reported for conventional 3×3 mm^2 scintillating crystal arrays (∼10 %). This difference can be explained by the detector geometry and readout configuration: the long (30 mm), narrow (2.05 mm) LFS crystals exhibit a higher aspect ratio, leading to longer photon transport paths, increased internal reflections, and greater light losses before reaching the photosensors (Liu *et al* 2022). The close packing of these slender crystals, combined with SMPPCs reading multiple crystals simultaneously, also increases ICS and optical crosstalk, further broadening the energy distribution. Nevertheless, our proposed detector was optimized primarily for timing and spatial characterization rather than energy performance.

The full-spectrum energy calibration was only performed to enable accurate performance reporting. Performing full-spectrum energy correction at the crystal level is an extremely time- and labor-intensive process. The gamma rays from low-energy sources are often inadequately penetrating the deeper layers, making it difficult to identify and separate photopeaks from scattered components. This challenge is further compounded for non-positron-emitting sources, where coincidence collimation techniques are not applicable. Fortunately, this comprehensive correction is not required for routine calibration, as the 511 keV photopeak is consistently identifiable and well-isolated in the ToT spectrum (see figure 8(a)). Thus, the acceptance energy window can be simply extracted by fitting a Gaussian function to the 511 keV photopeak on ToT spectrum. However, the full-spectrum energy correction is required for inter-layer scatter correction, which makes it the main bottleneck in implementing such techniques.

4.5. Z-positioning

In dual-readout detectors, determining the interaction point between the two readout ends remains a major challenge. Conventional approaches typically rely on labor-intensive calibration procedures in which each crystal is irradiated at multiple positions to generate dedicated calibration curves that correct for light compression, non-linear detector response, and variations in spatial resolution along the crystal length. When scaled to imaging systems containing hundreds or thousands of crystals, this procedure becomes increasingly demanding in terms of time and effort. Consequently, only a small subset of detectors is often fully calibrated, and the resulting calibration parameters are then applied to the remaining detectors. While this reduces calibration time substantially, it can introduce systematic inaccuracies and lead to degraded overall performance.

To address this limitation, we implemented three key design and methodological adaptations to perform our Z-positioning with a flood-based calibration method. (1) Introduction of the $\mathrm{ToT_{comb}}$ parameter: This composite parameter integrates two complementary sources of information, including the signal-amplitude difference between the crystal ends ($\mathrm{ToT_{diff}}$) and the signal-amplitude range on each end ($\mathrm{ToT_{N\_range}}$ and $\mathrm{ToT_{S\_range}}$). Incorporating this combined metric mitigated the degradation in resolution for events occurring near the crystal ends and resulted in a relatively uniform Z-resolution across the crystal length. Supplementary figures 6 and 10(c), (d), provide a comparison of detector's resolution when $\mathrm{ToT_{diff}}$ alone and alternatively $\mathrm{ToT_{comb}}$ was used for Z-positioning, respectively. (2) LUT-based Z-calibration: Assuming a uniform event distribution along the crystal length under flood irradiation, the $\mathrm{ToT_{comb}}$ range was divided into equally populated segments. The boundaries of these segments were used as a LUT to map the $\mathrm{ToT_{comb}}$ to the Z-positions. This binning method effectively compensates for light compression and non-linearities in positioning along the crystal (figure 10(b)). (3) Side-irradiation configuration: Finally, the proposed detector design enables uniform irradiation of all crystals along their length without detaching the detector blocks from the imaging system, allowing full-panel Z-positioning calibration using a single flood-illumination data acquisition.

The slit phantom test yielded average Z-position resolutions of 3.78, 3.84, 4.01, and 4.78 mm FWHM for layers 1 through 4, respectively. The degradation in resolution observed in the deeper layers is primarily attributed to a higher fraction of photons that have undergone Compton or Rayleigh scattering in the preceding layers. In addition, the reduced number of primary gamma photons reaching the deepest layer, resulting in limited event statistics, also contributes to the observed loss of resolution. It is important to note that the experiment was performed under realistic imaging conditions, with the slit placed on a 7 mm-thick radiolucent carbon-fiber bed, creating a 22 mm distance between the slit and the detector surface (figure 10(a)). This geometry introduces additional scattering, which likely caused a systematic degradation of the measured resolutions by a few percent compared with idealized laboratory setups.

4.6. Dual-readout detector design

(Liu *et al* (2022) developed dual-ended readout detectors with various sizes of LYSO crystal, and in the one with crystals sized 2.98 × 2.98 × 30 mm^3, coupled to two 4 × 4 arrays of 6 × 6 mm^2 SiPMs read out by ultrafast NINO ASICs, achieved an energy resolution of 12.1%, a DOI resolution (deal-readout positioning) of 3.9 mm, and a CTR of 214 ps. In another study, Jung *et al* (Jung *et al* 2024) implemented an 8 × 8 array of 1.9 × 1.9 × 15 mm^3 LYSO crystals, interfaced with the PETsys TOFPET2 evaluation kit, and reported a DOI resolution of 1.7 mm and a CTR of 299 ps. Similarly, Wang *et al* 2025) used an 8 × 8 array of 3.1 × 3.1 × 20 mm^3 LYSO crystals, coupled on both ends to Hamamatsu 8 × 8 SiPM arrays in a one-to-one crystal–SiPM configuration. The detectors were read out using PETsys TOFPET2 electronics and achieved a CTR of 234 ± 7 ps, an energy resolution of 13.7 ± 2%, and a DOI resolution of 2.6 ± 0.2 mm. Compared to their design, our detector showed superior timing performance (CTR of ∼200 ps vs 234 ps) while using longer crystals (30 mm vs 20 mm). In addition, for a similar active detection area and depth, our configuration requires 32 SMPPCs and 64 readout channels per detector tower, whereas their detector block requires 128 SiPMs and readout channels. This results in a significant reduction in both electronic complexity and manufacturing cost for scaled systems. Regarding dual-readout positioning (DOI in their case and axial positioning in ours), their detector achieved finer spatial resolution, mainly due to adoption of shorter crystals. However, their design relies on point-by-point irradiations for DOI calibration, while in contrast, our approach uses a simple flood-based calibration, offering a more practical and scalable solution for larger detector assemblies. It should also be noted that the mentioned studies were conducted using isolated detector blocks, often paired with a single reference detector for timing measurements. While effective for benchmarking purposes, such setups may not reflect the true performance in scaled configurations under realistic data acquisition conditions, where factors, such as crosstalk, inter-block scatter, bed scattering, and environmental influences, become significant.

A limitation of the dual-readout designs is the increased cost, as it requires twice the number of photodetectors and readout channels compared to single-ended configurations. This trade-off is more acceptable in the context of organ- or dedicated PET scanners, which typically feature compact geometries and fewer detector modules, thereby preventing an intolerable increase in overall manufacturing cost. Furthermore, as previously discussed, our design significantly reduced the required number of readout electronic channels compared to detectors with same size and a one-to-one crystal–SiPM configuration (Wang *et al* 2025). Another promising avenue is signal multiplexing techniques to reduce the number of required electronic channels without significantly compromising performance (Pourashraf *et al* 2024).

The axial attachment of the photodetectors used in our design introduces a potential limitation, as it creates gaps between adjacent detector towers. These inter-tower gaps reduce the overall sensitivity of the imaging system and if not treated may create artifacts and spatial non-uniformities in reconstructed images. Potential solutions include mechanical translation of the panels using motorized stages to fill the gaps through sequential acquisition, or the implementation of gap-filling algorithms during image reconstruction to compensate for the missing data (Huang *et al* 2021). Additionally, the DOI capability of the detector can partially alleviate this effect, as many oblique LORs traverse the gaps and get detected in upper layers of the detector, without compromised accuracy due to parallax effect.

5. Conclusion

In this study, we presented a compact, ready-to-use detector panel specifically designed for organ- and purpose-dedicated PET scanners, based on a state-of-the-art 4-layered dual-readout architecture. By incorporating a multi-layer detector design and ultrafast readout electronics, the panel demonstrated excellent DOI and TOF performance. A comprehensive evaluation was conducted under realistic data acquisition conditions, highlighting the detector's robustness, scalability, and suitability for practical applications. Particular emphasis was placed on developing a streamlined calibration method, enabling efficient deployment in full-scale scanner assemblies. We believe that our developed DOI-TOF detector panel can open venues for development of next generation dedicated PET scanners, supporting novel scanner geometries while ensuring uniform, high-quality imaging performance across the entire field-of-view.

Data availability statement

The data cannot be made publicly available upon publication because they are not available in a format that is sufficiently accessible or reusable by other researchers. The data that support the findings of this study are available upon reasonable request from the authors.

Supplementary material available at https://doi.org/10.1088/1361-6560/ae2b4a/data1.

Acknowledgments

This work was supported by the Eurostars program of the European Commission under Grant E! 114021 ProVision and the Private Foundation of Geneva University Hospitals under Grant RC-06–01.

Conflict of interest

The authors declare that they have no known competing financial interests or personal relationships that could have appeared to influence the work reported in this paper.

Author contributions

Abdollah Saberi Manesh 0000-0001-7327-2558
Conceptualization (equal), Data curation (equal), Formal analysis (equal), Investigation (equal), Methodology (equal), Software (equal), Validation (equal), Writing – review & editing (equal)

Katayoun Doroud
Conceptualization (supporting), Funding acquisition (supporting), Investigation (equal), Resources (supporting), Writing – review & editing (equal)

Hossein Arabi 0000-0001-6526-0960
Conceptualization (equal), Data curation (equal), Formal analysis (equal), Software (equal), Validation (equal), Writing – review & editing (equal)

Habib Zaidi 0000-0001-7559-5297
Conceptualization (lead), Data curation (lead), Formal analysis (lead), Funding acquisition (lead), Investigation (lead), Methodology (lead), Software (lead), Supervision (lead), Writing – review & editing (equal)

References

Amini M, Saberi-Manesh A, Arabi H, Doroud K, Williams C and Zaidi H 2024 Inter-layer Compton scatter recovery in provision-PET: a prostate dedicated PET scanner with four layered dual-readout PET detector modules *J. Nucl. Med.* **65** 242240 (available at: https://jnm.snmjournals.org/content/65/supplement_2/242240)

Borghi G, Peet B J, Tabacchini V and Schaart D R 2016 A 32 mm× 32 mm× 22 mm monolithic LYSO: CE detector with dual-sided digital photon counter readout for ultrahigh-performance TOF-PET and TOF-PET/MRI *Phys. Med. Biol.* **61** 4929

Catana C 2019 Development of dedicated brain PET imaging devices: recent advances and future perspectives *J. Nucl. Med.* **60** 1044–52

Cates J W and Levin C S 2018 Evaluation of a clinical TOF-PET detector design that achieves⩽ 100 ps coincidence time resolution *Phys. Med. Biol.* **63** 115011

Conti M and Bendriem B 2019 The new opportunities for high time resolution clinical TOF PET *Clin. Transl. Imaging* **7** 139–47

Doroud K, Kim D, Kwon K, Liu Z, Min B, Williams M and Zichichi A 2021 The strip SiPM: a study of single photon time resolution *J. Instrum.* **16** 06017

Doroud K, Rodriguez A, Williams M, Zichichi A and Zuyeuski R 2014 *2014 IEEE Nuclear Science Symp. and Medical Imaging Conf. (NSS/MIC)* Vol Series (IEEE) pp 1–4

El Ouaridi A, Ait Elcadi Z, Mkimel M, Bougteb M and El Baydaoui R 2024 The detection instrumentation and geometric design of clinical PET scanner: towards better performance and broader clinical applications *Biomed. Phys. Eng. Express* **10** 032002

Gonzalez A J and Gonzalez-Montoro A 2024 Gonzalez A J and Gonzalez-Montoro A 2024 Developments in dedicated prostate PET instrumentation *PET Clin.* **19** 49–57

Gonzalez-Montoro A *et al* 2022 A new brain dedicated PET scanner with 4D detector information *Bio-Algorithms Med-Syst.* **18** 107–19

Gonzalez-Montoro A, Gonzalez A J, Pourashraf S, Miyaoka R S, Bruyndonckx P, Chinn G, Pierce L A and Levin C S 2021 Evolution of PET detectors and event positioning algorithms using monolithic scintillation crystals *IEEE Trans. Radiat. Plasma Med. Sci.* **5** 282–305

Huang Y, Zhu H, Duan X, Hong X, Sun H, Lv W, Lu L and Feng Q 2021 Gapfill-recon net: a cascade network for simultaneously pet gap filling and image reconstruction *Comput. Methods Programs Biomed.* **208** 106271

Jung J H, Choi Y, Yun J, Jung J and Lee S 2024 Effects of reflector, surface treatment, and length of scintillation crystal on the performance of TOF-DOI PET detector with dual-ended readout *Nucl. Eng. Technol.* **56** 2633–40

LaBella A, Cao X, Zeng X, Zhao W and Goldan A H 2021 Sub-2 mm depth of interaction localization in PET detectors with prismatoid light guide arrays and single-ended readout using convolutional neural networks *Med. Phys.* **48** 1019–25

Lee M S, Shim H S and Lee J S 2024 Strategies for mitigating inter-crystal scattering effects in positron emission tomography: a comprehensive review *Biomed. Eng. Lett.* **14** 1243–58

Liu Z, Niu M, Kuang Z, Ren N, Wu S, Cong L, Wang X, Sang Z, Williams C and Yang Y 2022 High resolution detectors for whole-body PET scanners by using dual-ended readout *EJNMMI Phys.* **9** 29

Mohammadi A, Takyu S, Nishikido F, Yoshida E, Shimizu K, Sakai T and Yamaya T 2019a Development of a dual-end detector with TOF and DOI capabilities using crystal bars segmented by subsurface laser engraving *Nucl. Instrum. Methods Phys. Res. A* **931** 236–41

Mohammadi I, Castro I, Correia P, Silva A and Veloso J 2019b Minimization of parallax error in positron emission tomography using depth of interaction capable detectors: methods and apparatus *Biomed. Phys. Eng. Express* **5** 062001

Moses W W 2011 Fundamental limits of spatial resolution in PET *Nucl. Instrum. Methods Phys. Res. A* **648** S236–S40

Pizzichemi M, Polesel A, Stringhini G, Gundacker S, Lecoq P, Tavernier S, Paganoni M and Auffray E 2019 On light sharing TOF-PET modules with depth of interaction and 157 ps FWHM coincidence time resolution *Phys. Med. Biol.* **64** 155008

Pourashraf S, Cates J, Innes D and Levin C 2024 Front-end electronics for a 100 ps coincidence time resolution TOF-PET detector with 24-fold LVDS timing channel multiplexing *IEEE Trans. Instrum. Meas.* **73** 1–14

Razdevšek G, Fakhri G E, Marin T, Dolenec R, Orehar M, Chemli Y, Gola A G, Gascon D, Majewski S and Pestotnik R 2025 Flexible and modular PET: evaluating the potential of TOF-DOI panel detectors *Med. Phys.* **52** 2845–60

Sanaat A, Amini M, Arabi H and Zaidi H 2024 The quest for multifunctional and dedicated PET instrumentation with irregular geometries *Ann. Nucl. Med.* **38** 31–70

Schaart D R 2021 Physics and technology of time-of-flight PET detectors *Phys. Med. Biol.* **66** 09TR1

Seo M, Park H, Lee S, Ko G B and Lee J S 2023 Depth-of-interaction positron emission tomography detector with 45° tilted silicon photomultipliers using dual-ended signal readout *Med. Phys.* **50** 4112–21

Shibuya K, Yoshida E, Nishikido F, Suzuki T, Tsuda T, Inadama N, Yamaya T and Murayama H 2007 Annihilation photon acollinearity in PET: volunteer and phantom FDG studies *Phys. Med. Biol.* **52** 5249

Surti S and Karp J S 2020 Update on latest advances in time-of-flight PET *Phys. Med.* **80** 251–8

Venturini Y, Maggio C, Tintori C, Ninci D, Mati A, Picchi A, Abba A, Locatelli M, Williams C and Williams T 2024 *2024 IEEE Nuclear Science Symp. (NSS), Medical Imaging Conf. (MIC) and Room Temperature Semiconductor Detector Conf. (RTSD) vol Series* (IEEE) pp 1

Wang F, Kao C-M, Zhang X, Liu L, Hua Y, Kim H, Choong W-S and Xie Q 2024 DOI-and TOF-capable PET array detector using double-ended light readout and stripline-based row and column electronic readout *IEEE Trans. Radiat. Plasma Med. Sci.* **8** 269–76

Wang H, Xie J and Du J 2025 Development of whole-body TOF-DOI PET detector using dual-ended readout method *IEEE Trans. Instrum. Meas.* **74**

Watanabe M, Moriya T, Uchida H and Omura T 2021 Simulation study of potential time-of-flight capabilities for a multilayer DOI-PET detector with an independent readout structure *Phys. Med. Biol.* **66** 18NT02

Weindel K, Nadig V, Herweg K, Schulz V and Gundacker S 2023 A time-based double-sided readout concept of 100 mm LYSO: Ce, Ca fibres for future axial TOF-PET *EJNMMI Phys.* **10** 43

Yoshida E, Obata F and Yamaya T 2024 Timing estimation of the exponentiated energy-weighted average for crosshair light sharing TOF-DOI PET detector *Nucl. Instrum. Methods Phys. Res. A* **1059** 168949

Yoshida E and Yamaya T 2024 PET detectors with depth-of-interaction and time-of-flight capabilities *Radiol. Phys. Technol.* **17** 596–609

Zaidi H, Surti S and Alavi A 2024 Innovations in organ-specific PET instrumentation: quo vadis *PET Clin.* **19** xi–xii

Zatcepin A and Ziegler S I 2023 Detectors in positron emission tomography *Z. Med. Phys.* **33** 4–12